PAPER

Check for updates

Armor-like passivated CsPbBr₃ quantum dots: boosted stability with hand-in-hand ligands and enhanced performance of nuclear batteries†

Dandan Yang,‡[a] Zhiheng Xu, [ID] ‡[b] Chunhui Gong, [ID] [c] Lin Su,[d] Xiaoming Li, [ID] *[a]
Xiaobin Tang,[b] Dongling Geng,[a] Cuifang Meng,[a] Feng Xu [ID] [d] and Haibo Zeng [ID] *[a]

One of the main reasons for the stability issue of inorganic perovskite quantum dots (PQDs) is the fragile protection of surface ligands. Here, an armor-like passivation strategy is proposed to improve the comprehensive stability of PQDs *via* a solvothermal fabrication method. That is, forming an armor-like protection layer for every single surface point by introducing coupling ligands with strong affinity (both L and X type ligands). The interactions between ligands *via* hydrogen bonds and strong affinity of ligands to surface atoms are evidenced by [1]H-nuclear magnetic resonance measurements and Fourier transform infrared spectroscopy. As a result, long-term storage stability, high quantum yield, good water resistance, and good radiation hardness of PQDs are achieved. More than 60% of the radioluminescence intensity of the PQD film could be retained under continuous irradiation of 42 kGy. The output power can even be increased by 34.48% compared with the battery without PQD film. This armor-like passivation strategy also provides good reference for the stability improvement of both light-emitting and photovoltaic devices.

Introduction

As a representative of miniaturized nuclear batteries, radioluminescent nuclear batteries (RLNBs) have been widely studied in recent years. Radioluminescent materials are the core energy conversion component, and their performance seriously restricts the development of battery technology. Inorganic halide perovskite quantum dots (PQDs) have attracted widespread attention due to their high photoluminescence quantum yield (PLQY) and tunable emission, which are expected to become key materials for the next generation of RLNBs.[1–3] By virtue of their spectral optimization and regulation characteristics, PQDs can couple the components of the RLNBs quite well and enhance the performance.[4–6] Generally, the long-term stability of the battery in dissimilar environments mainly depends on the energy conversion material, so the stability and reliability of perovskite QDs connecting the above and the below layers are particularly critical.

Despite the recent progress made in the surface states of CsPbX₃ QDs, how to select ligands for improving the long-term stability of QDs is still challenging. CsPbBr₃ QDs prepared using weak binding ligands usually fall off inevitably during the separation and purification processes, resulting in defect energy levels in the band gap[7] and poor stability. Therefore, X-type ligand, dual ligand[8–10] and multiple ligand[11,12] passivation strategies have been proposed to improve the optical properties and stability of the perovskite QDs.[7,13–15] Recently, as a kind of ligands with large steric hindrance and free protonation, quaternary ammonium salts (RNH₄⁺) have often been used to ensure the high colloidal stability of perovskite QDs.[16–18] For instance, Shynkarenko *et al.* reported a direct synthesis of didodecyldimethylammonium halide (DDAX)-stabilized CsPbX₃ QDs.[19] DDAX as the sole ligand dissolves lead bromide together with mesitylene, but a relatively low PLQY was obtained. The phenomenon was attributed to the reduction of surface coverage and increment of the surface dangling bonds. Besides, an amine-free method has been developed to prepare stable CsPbBr₃ QDs in recent years. Sargent's group proposed a total OA strategy to prepare stable CsPbX₃ QDs.[20] The deprotonated OA as a stabilizer coordinates with lead ions to enhance the purification stability. But carboxylic acid as a weak acidic ligand could still easily fall off, resulting in some halogen vacancies and reducing the storage stability.[21] To further illustrate the

[a]*MIIT Key Laboratory of Advanced Display Materials and Devices, Institute of Optoelectronics & Nanomaterials, College of Materials Science and Engineering, Nanjing University of Science and Technology, Nanjing 210094, China. E-mail: lixiaoming@njust.edu.cn; zeng.haibo@njust.edu.cn*

[b]*Department of Nuclear Science and Technology, Nanjing University of Aeronautics and Astronautics, Nanjing 211106, China*

[c]*School of Environmental and Biological Engineering, Nanjing University of Science and Technology, Nanjing 210094, China*

[d]*SEU-FEI Nano-Pico Center, Key Laboratory of MEMS of Ministry of Education, Southeast University, Nanjing 210096, China*

† Electronic supplementary information (ESI) available: Experimental part, absorbance and PL spectra, XRD and TEM, ^{1}H NMR patterns, FTIR pattern, XPS spectra, radioluminescence test, and additional figures and tables. See DOI: 10.1039/d0ta12365j

‡ D. Yang and Z. Xu contributed equally.

effect of a sole ligand on the stability of QDs, Zhang *et al.* revealed that alkyl phosphoric acid as the only ligand can contribute to near unity PLQY and enhance the colloidal stability of CsPbBr$_3$ QDs.[22–24] But the stability of CsPbBr$_3$ QDs was not further discussed in this work. Compared with alkyl phosphate ligands, alkylbenzenesulfonic acid has stronger acidity and electron withdrawing ability, and can form strong binding with the surface of perovskite QDs.[25] But this strategy requires the introduction of too much 4-dodecylbenzene-sulfonic acid (4-DBSA) to dissolve inorganic salts, which affects the crystallinity and phase stability of CsPbBr$_3$ QDs. In short, strategies to obtain perovskite QDs with high efficiency and long-term stability are still not satisfied so far.

Hence, we report an armor-like passivation strategy to synthesize highly efficient and stable CsPbBr$_3$ QDs by a simple solvothermal method. The protective layer formed by hand-in-hand ligands, and the electrostatic adsorption formed by ammonium salts with large steric hindrance endow the passivated CsPbBr$_3$ QDs (DP-QDs) with storage stability for more than three months and 97 ± 3% QY. Meanwhile, the DP-QDs retained 90% of PLQY and phase stability after three months, and showed a high resistance against water treatment for a month. Taking advantage of the excellent optical properties and good stability, we further demonstrated that the RL intensity of the prepared DP-QD film remained above 63.9% under the condition of an average photon energy of 1.25 MeV and a total dose of about 42 kGy. The output power of the nuclear battery based on the DP-QD film could be increased by 26.96% compared with the conventional OAm-film, and by 34.48% compared with that without the film. All these results showed that the DP-QDs with high stability and RL efficiency passivated by hand-in-hand ligands provide application potential for nuclear batteries with ultra-high reliability for deep space or underwater exploration missions.

Experimental section

Synthesis of DP-QDs

PbBr$_2$ (0.27 mmol, 0.1 g), ODE (8 mL), *tert*-butylbenzene (5 mL), DDAB (75 mg), OAm (0.35 mL) and CsDBSA (0.6 mL) were loaded into a 50 mL Teflon-lined autoclave, and then reacted at 150 °C in a rolling oven for 1 h. Ethyl acetate was added into the crude solution with a volume ratio of 1 : 3 and the mixture was centrifuged for 1 min at 9000 rpm. The purification procedures were repeated another time. The precipitate was dispersed in 2 mL of toluene to obtain a clear solution.

Perovskite film and PV module

The quantum dot solution is mixed with polymethyl metha-crylate (PMMA) according to the mass ratio of 1 : 3 by the blending method, and the mixture is uniformly stirred and then dried and cured at room temperature in a vacuum chamber, and taken out after formation. In this study, GaAs-based and AlGaInP-based PV modules, which have been surface-modified by the antireflection film, were used as the photoelectric conversion units of RLNBs respectively. The effective working area of PV modules is 1 cm^2, so the perovskite film is also trimmed to a uniform thickness and a size of 1 cm × 1 cm. The perovskite film is closely attached to the light-receiving surface of the PV module.

Results and discussion

DBSA-QDs with high quantum efficiency and purification stability were reported in our previous work.[25] In the synthesis system, excessive DBSA ligands can destroy the crystallization and phase stability of CsPbBr$_3$ QDs. Thus, CsDBSA is used as a precursor to prepare CsPbBr$_3$ QDs in this work. The detailed reaction process involves mixing PbBr$_2$, an aliphatic amine, CsDBSA and DDAB with *tert*-butylbenzene, then reacting at 150 °C, and finally obtaining the bright green DP-QDs (Fig. S1†). If DDAB is used as a single ligand, it will decrease the solubility of CsPbBr$_3$ QDs and leads to a large number of aggregated particles (Fig. S2†) and partial CsPb$_2$Br$_5$ phase (Fig. S3†). Manna *et al.* proved that too much DDAB could destroy the stability of QDs,[16] so a small amount of DDAB was selected as a phase transfer catalyst to dissolve PbBr$_2$ and some primary amines were used as auxiliary ligands to stabilize CsPbBr$_3$ QDs. Finally, the high-quality DP-QDs are obtained by purification twice for later use. Specifically, as a phase transfer catalyst, DDAB can first dissolve a small amount of lead bromide, and the disso-ciated lead ions will coordinate with the π electrons of the *tert*-butylbenzene ring, which promote the transfer of PbBr$_2$ to the organic phase and finally completely dissolve PbBr$_2$. Instead of CsDBSA, CsOA is used as a comparative example to investigate the optical properties and surface states of CsPbBr$_3$ QDs.

The CsOA-QDs and DP-QDs have similar morphology and crystal phase, as seen from transmission electron microscopy (TEM, Fig. 1a and S4†) images and X-ray diffraction (XRD, Fig. 1b) patterns. From the TEM and size distribution histo-gram, monodisperse DP- and CsOA-QDs with an average edge length of 9.3 nm and 10.3 nm are obtained, respectively (Fig. S5†). The high-resolution TEM and fast Fourier transform (FFT) images indicate an interplanar spacing of 2.95 nm, which is in good accordance with the (002) crystal planes of cubic CsPbBr$_3$ QDs.[26] Meanwhile, they have similar full-width at half-maximum (FWHM) of 17 nm (Fig. 1c). However, compared with CsOA-QDs, DP-QDs show a sharper exciton absorption peak, which is consistent with the corresponding particle size, and the phenomenon is attributed to the quantum size effect.[27,28] Moreover, the CsOA-QDs and DP-QDs were diluted to a certain concentration, and the PLQYs measured by the integrating sphere were 69 ± 3% and 97 ± 3%,[29] respectively. Corre-spondingly, Fig. 1d indicates that the fluorescence lifetime of DP-QDs can be fitted by double-exponential decay and an average lifetime of 7.58 ns is obtained. In contrast, the CsOA-QDs exhibit a double exponential decay and the average life-time is 6.93 ns. The average lifetime of CsOA-QDs is short, indicating the deviation of the recombination pathways due to defects.[7] Therefore, compared with OA, DBSA and OAm as strong binding ligands have better manipulation ability on exciton recombination and effectively eliminate the defect state.
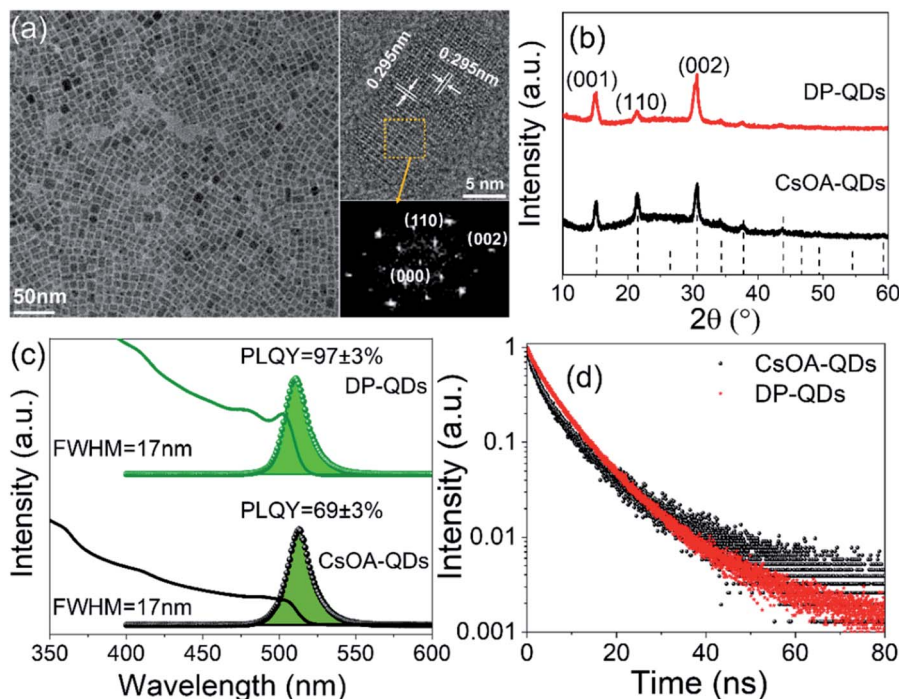
This journal is © The Royal Society of Chemistry 2021

J. Mater. Chem. A, 2021, **9**, 8772–8781 | **8773**

Fig. 1 Crystal structure and optical properties of PQDs. (a) TEM, HRTEM images and selected area FFT pattern of DP-QDs. (b) Powder XRD patterns, (c) absorption and PL spectra, and (d) PL decay curves of CsOA- and DP-QDs with an excitation wavelength of 380 nm.

Meanwhile, DDAB also improves the stability and enhances the PLQY of $CsPbBr_3$ QDs.

As is known to all, the microstructure of QDs determines their macroscopic properties. Taking $CsPbBr_3$ QDs as an example, the surface state of OAm-QDs is mainly formed by hydrogen bonds between protonated amine ions and surface bromine ions (Scheme 1a, OAm-QDs). The hydrogen bonds weaken the coulomb interaction between lead ions and bromine ions, causing amine ions on the surface of QDs to fall off and form surface dangling bonds further.[30] This leads to the non-radiative channels for exciton recombination of QDs, thus reducing the efficiency and stability of QDs. Therefore, it is necessary to introduce ligands with matching electronic properties to passivate the surface electronic defects of QDs. As a widely used surface ligand, DDAB is employed to improve the stability of $CsPbBr_3$ QDs herein, which has certain significance in designing stable QDs (Fig. S6†).[31] However, due to its steric hindrance, the surface coverage can be reduced and the optical performance can be affected. Therefore, the armor-like passivation strategy with continuous hydrogen bonds was used here. At the same time, the long-branched chain of the DDA^+ ligand can protect the QDs from external damage (Scheme 1c, DP-QDs).

In order to verify the binding interactions of inter-ligands and ligands on the surface atoms of QDs, ^{1}H-nuclear magnetic resonance (NMR) measurements, Fourier transform infrared spectroscopy (FTIR) and X-ray photoelectron spectroscopy (XPS) were carried out to investigate the surface chemical states of QDs. To analyze the interactions between surface ligands and QDs, the ^{1}H NMR resonance spectra of free DBSA

and CsDBSA precursors were first detected as shown in Fig. S7.† From the ^{1}H NMR spectrum, 1-OH ^{1}H resonances of DBSA appeared at 11.5 ppm, while it was completely eliminated in the CsDBSA precursor, implying that DBSA could completely react with Cs^+ anions and would not protonate OAm. Fig. 2a shows the ^{1}H NMR resonances of the CsOA-QDs and DP-QDs, which showed a broader signal peak at 3.47 ppm compared with DDAB-QDs (Fig. S8†), confirming the interaction of DDAB between the surface Pb atoms. Besides, the 3-CH_2 ^{1}H resonance of DP-QDs appeared at 2.49 ppm, indicating the existence of unprotonated OAm on the surface. By contrast, the resonance peak at 2.49 ppm of CsOA-QDs was very weak, which indicated that less unprotonated OAm existed in CsOA-QDs.

Considering that the benzenesulfonate ions have three oxygen atoms, it is speculated that they may form continuous N–H⋯O hydrogen bonds with unprotonated OAm. So, tri-octylphosphine oxide (TOPO), tributylphosphine oxide (TBPO) and triphenylphosphine oxide (PhOP) ligands with different steric hindrances were used to exchange the OAm ligands and explore the surface states of DP-QDs. Interestingly, the 3-CH_2 ^{1}H resonance peak at 2.47 ppm of TOPO-QDs becomes stronger than that of DP-QDs, implying that TOPO breaks the intrinsic surface states and promotes the binding of more unprotonated OAm to the Pb cations. In addition, TOPO may not be able to replace OAm because of the large steric hindrance. Thus, TBPO and PhOP ligands with lower steric hindrance were used. As a result, the resonance peak at 2.47 ppm of TBPO-QDs and PhOP-QDs decreases gradually, revealing the breakage of continuous N–H⋯O bonds and the replacement of unprotonated OAm ligands with TBPO and PhOP. Based on the above

8774 | J. Mater. Chem. A, 2021, 9, 8772–8781

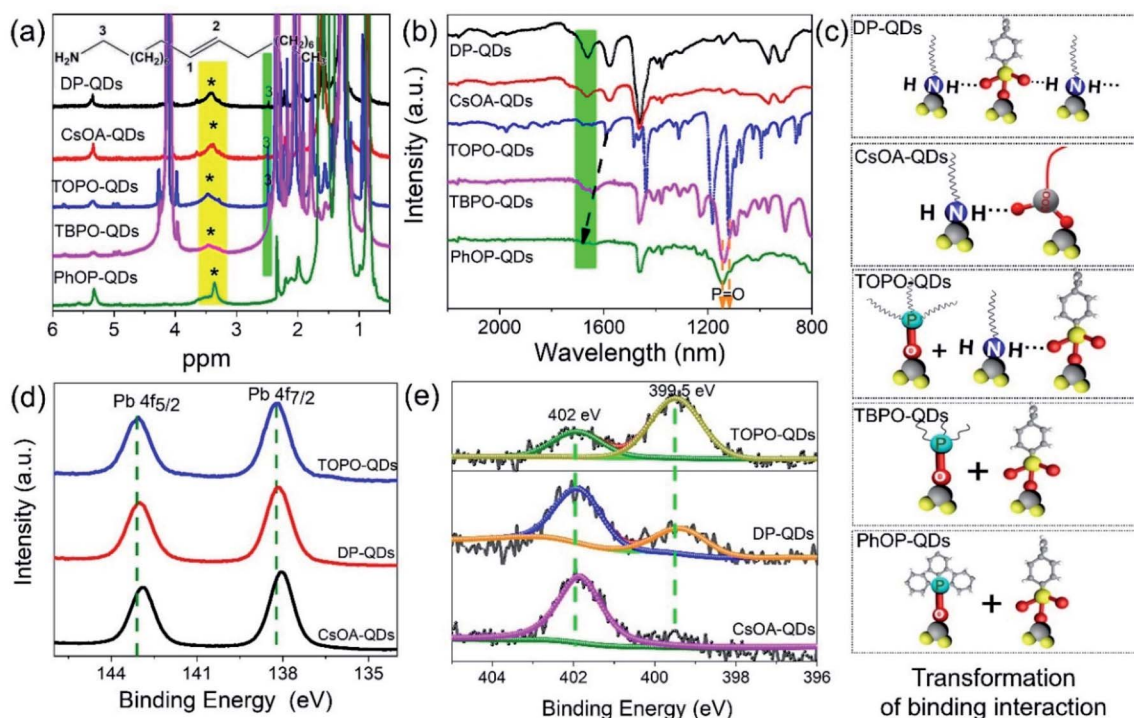This journal is © The Royal Society of Chemistry 2021
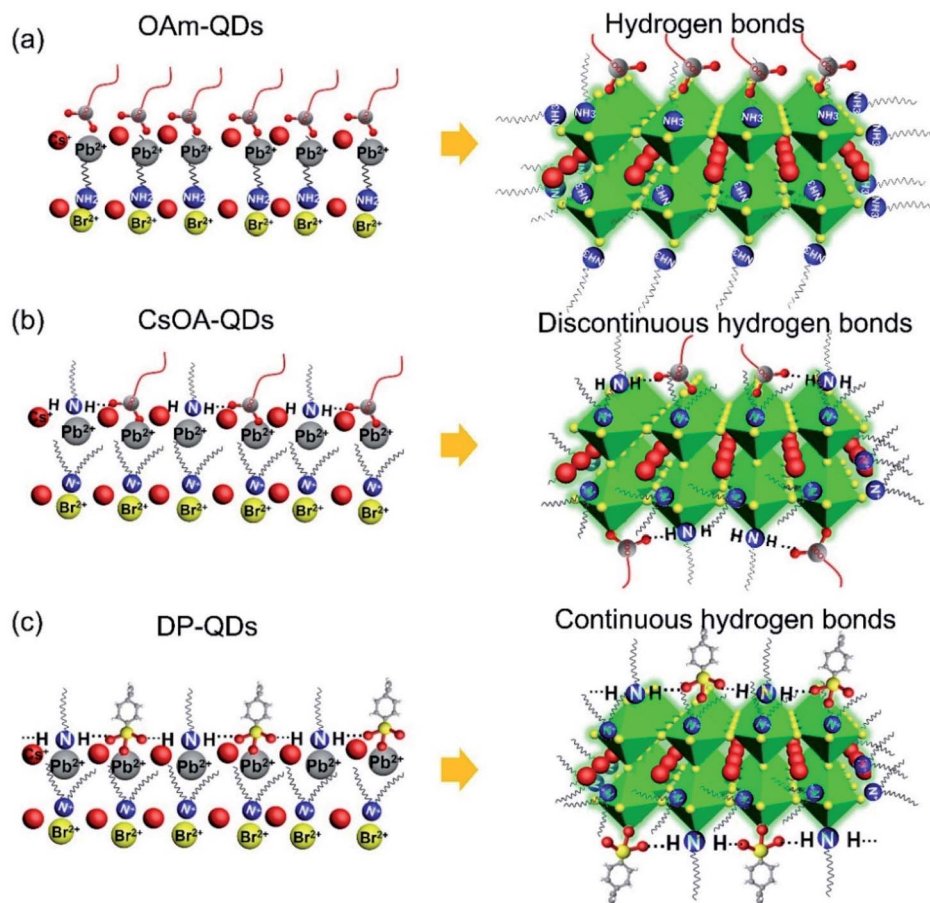
Scheme 1 Illustration of possible surface states of OAm-QDs, CsOA-QDs and DP-QDs. (a) The formation of weak hydrogen bonds by OAm with bromine. (b) Discontinuous hydrogen bonds formed by an oxygen atom of OA and unprotonated OAm and electrostatic adsorption between DDA⁺ and bromine. (c) Armor-like layer for every single surface point by introducing unprotonated OAm and DBSA ligands with strong affinity. These ligands not only possess strong interaction with PQDs, but also interact with each other via hydrogen bonds.

analyses, the continuous N–H⋯O bonds formed by hand-in-hand ligands exist on the surface of DP-QDs (Fig. 2c, DP-QDs).

To further confirm the inter-ligand interaction, FTIR measurements of CsOA- and DP-QDs were conducted in Fig. 2b. The expected absorption peaks at 1661 cm^{-1} and 1578 cm^{-1} can be attributed to the shear bending vibration of hydrogen-bonded N–H.[32,33] It is emphasized that the absence of N–H bonds in DDAB leads to no characteristic peaks (Fig. S9†). Compared with DP-QDs, the bending vibration intensity of CsOA-QDs is weak, which means the continuous N–H⋯O hydrogen bonds formed by the two oxygen atoms of DBSA and hydrogen atoms of OAm are stronger than the discontinuous N–H⋯O bonds formed by the oxygen atom of OA. That is to say, the discontinuous N–H⋯O bonds are more likely to form between OA and unprotonated OAm, resulting in weak binding interaction on the surface of CsOA-QDs (Fig. 2c, CsOA-QDs). In order to further illustrate this conjecture, the toluene solutions of TOPO, TBPO and PhOP ligands were used to exchange with DP-QDs. The FTIR results showed that the bending vibration peak of TOPO-treated QDs (TOPO-QDs) at 1660 cm^{-1} disappeared, and the stretching vibration peak of N–H at 1578 cm^{-1} blue-shifted to 1590 cm^{-1}. The absorption peak at 1590 cm^{-1} is attributed to the stretching vibration of –NH$_2$,

which is consistent with the ¹H NMR data, and it can be inferred that the introduction of TOPO breaks the continuity of N–H⋯O bonds, forming a discontinuous hydrogen bond between an oxygen atom of DBSA and hydrogen atoms of OAm (Fig. 2c, TOPO-QDs). It is worth mentioning that the stretching vibration of the P═O bonds shifted to the lower wavenumber (1119 cm^{-1}) for TOPO-QDs, compared with pure TOPO at 1143 cm^{-1} (Fig. S10†). The red-shift is due to the decreased force constant according to the harmonic motion of a diatomic model, which reveals that TOPO ligands bind to the Pb atoms.[34,35] The possible reason is that TOPO occupies the position of DDAB, which makes DDAB fall off, and TOPO can effectively interact with lead ions (Fig. 2c, TOPO-QDs). As neutral ligands with low steric hindrance, the shear bending vibrations of hydrogen-bonded N–H at 1660 cm^{-1} and 1578 cm^{-1} become one vibration peak at 1637 cm^{-1} and gradually weakened. Therefore, TBPO and PhOP almost changed the coordination mode of inter-ligands and exchanged with unprotonated OAm. As a result, TBPO and PhOP ligands can interact with lead atoms (Fig. 2c, TBPO-QDs and PhOP-QDs).

Based on the above ¹H NMR and FTIR analyses, the primary amines and 4-DBSA interact with lead ions as small compact ligands to form continuous hydrogen bonds, and quaternary

This journal is © The Royal Society of Chemistry 2021

J. Mater. Chem. A, 2021, **9**, 8772–8781 | **8775**

Fig. 2 Evidences of the interaction between ligands and ligands to the QD surface. (a) Selected regions of ^{1}H NMR spectra (molecular structural formula and location number of unprotonated OAm) and (b) FTIR results in the range of 2200 to 800 cm^{-1} of CsOA, DP, TOPO, TBPO and PhOP-QDs. (c) Continuous hydrogen bonds formed by two oxygen atoms and unprotonated OAm for DP-QDs, discontinuous hydrogen bonds formed by an oxygen atom of OA and unprotonated OAm for CsOA-QDs, the break of continuous hydrogen bonds for TOPO-QDs, substitution of hydrogen bond for TBPO- and PhOP-QDs. XPS spectra of (d) Pb 4f and (e) N 1s for CsOA, DP and TOPO-QDs.

ammonium salts interact with bromine ions to construct a protective layer, resulting in the formation of DP-QDs (Scheme 1c, DP-QDs). Compared with DP-QDs, CsOA-QDs have a similar protective layer formed by DDAB. However, the discontinuous hydrogen bonds formed between primary amines and OA, and the weak binding interaction of OA with lead ions, result in the decrease of stability of CsOA-QDs (Scheme 1b, CsOA-QDs).

Fig. 2d and e show the chemical states of the three samples. For CsOA-QDs, the Pb 4f core-level spectrum (Fig. 2d) shows peaks at 142.8 and 138 eV corresponding to $4f_{5/2}$ and $4f_{7/2}$, respectively. A shift of 0.16 eV was observed for DP-QDs and TOPO-QDs. The shift can be ascribed to the fact that more continuous N–H···O bonds bind to Pb atoms. Besides, benzenesulfonate ion has stronger electronegativity compared with the carboxylate ion.[25] For TOPO-QDs, although FTIR analysis proves that the oxygen atoms of P=O interact with lead atoms, the binding energy shift of lead atoms is consistent with the DP-QDs, indicating that TOPO ligands do not change the outer electron cloud density of lead atoms. The N 1s curves of DP- and TOPO-QDs are fitted with two peaks at 402 eV and 399.6 eV (Fig. 2e), which correspond to *tert*-ammonium cations from DDAB and unprotonated OAm, respectively. It further illustrates the presence of –NH$_2$ and DDA$^+$ group.[36] Compared with DP-QDs, the intensity of the N 1s core level of TOPO-QDs becomes weaker at the peak of 402 eV and stronger at the peak of 399.6 eV, which means that more –NH$_2$ groups are bound to the surface of QDs, and TOPO may cause some DDAB

ligands to fall off due to the large steric hindrance. For CsOA and DP-QDs, the O 1s core-level spectra have peaks at 532.1 eV, which indicates that OA and DBSA ligands exist on the surface of QDs. For TOPO-treated QDs, we also focused on the O 1s peak to monitor the role of TOPO. Fig. S11† shows the peak shift from 532.1 eV to the higher binding energy of 532.5 eV, and a new peak at 531.3 eV appears, which can be assigned to the binding interaction of TOPO ligands.[37] Through the above analyses, the continuous N–H···O bonds may act as a protective layer on the surface of DP-QDs, effectively reducing the surface dangling bonds, thereby attributing to a 97 ± 3% QY and longer fluorescence decay lifetime.

The surface ligand coordination mode of CsPbBr$_3$ QDs directly affects the surface dangling bond, surface coverage, solubility and stability. Optimizing the coordination mode of the surface ligands may be the key to improve their storage stability and water resistance. The storage stability and water resistance of OAm-QDs, CsOA-QDs and DP-QDs were tested after two purifications. When OAm-QDs were stored for 14 days, the PL peak red-shifted from 513 nm to 516 nm, forming a large number of yellow particles (Fig. S12†). It indicates that the formation of halogen vacancies leads to the agglomeration of QDs (Fig. S13†) and the phase transition to an orthorhombic structure (Fig. S14†). After three months of storage, the CsOA-QDs show a slight redshift and the PLQY decreases to 30%, while the PL peak of DP-QDs remains unchanged (Fig. S15a and b†), and more than 90% of the PLQY can be retained (Fig. 3d).
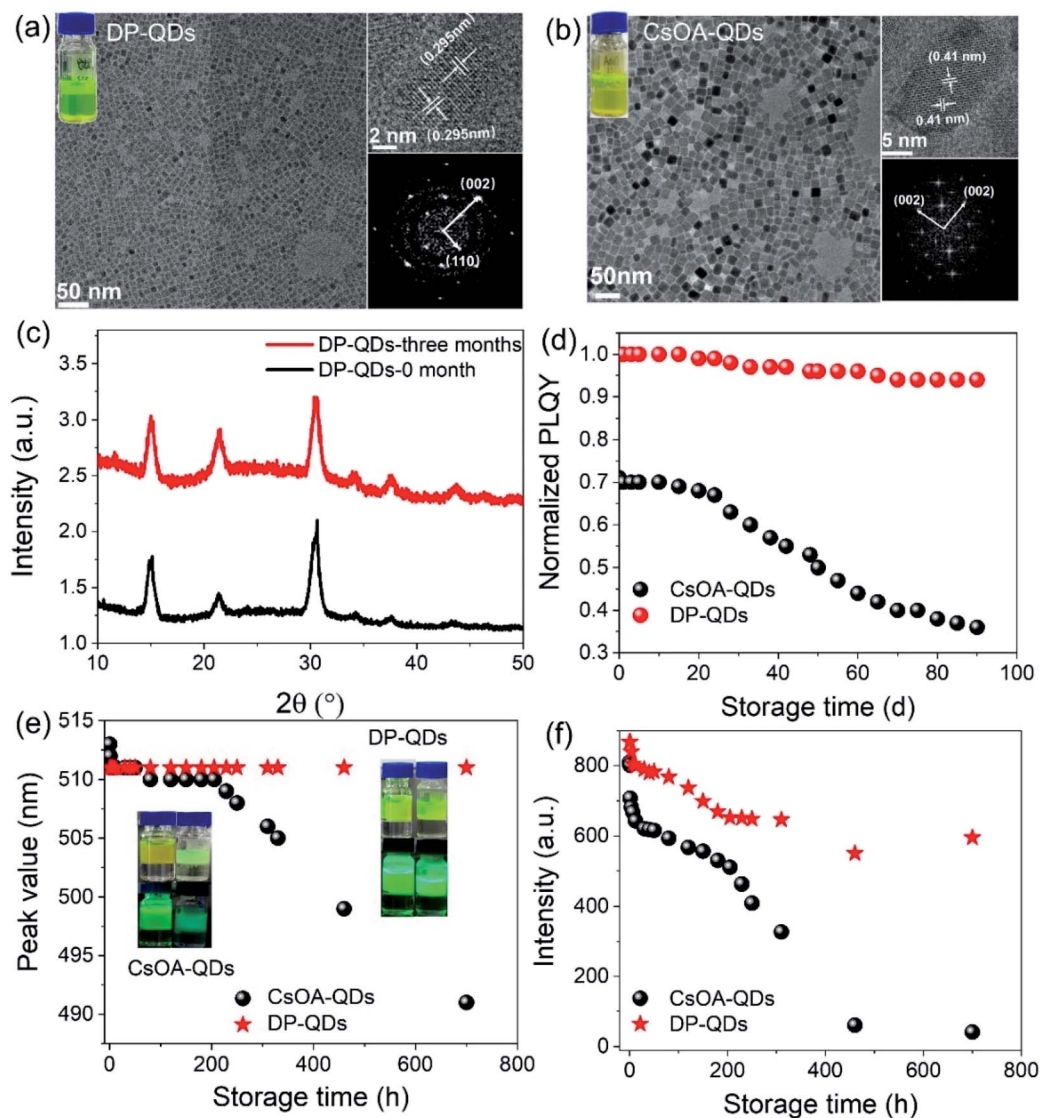
8776 | *J. Mater. Chem. A*, 2021, **9**, 8772–8781

This journal is © The Royal Society of Chemistry 2021

Fig. 3 Long-term storage, phase, and water stability of PQDs. TEM, HRTEM images and FFT pattern (a) DP and (b) CsOA-QDs aged for three months. (c) Powder XRD patterns and (d) PLQY of CsOA and DP-QDs after three months. (e) Peak wavelength and (f) PL intensity of CsOA and DP-QDs after water treatment under a static state (upper layer, hexane, bottom layer, water).

Furthermore, TEM, HRTEM images (Fig. 3a) and XRD patterns (Fig. 3c) show that the DP-QDs still retain the cubic phase after three months of storage, as well as the average size (9.15 nm, Fig. S15c†). For CsOA-QDs, the average size increased from 10.3 nm to 20.8 nm and the distribution was uneven (Fig. S15d† and 3b).

Water resistance of QDs was further exemplified. The hexane QD solution and deionized water were placed in a glass bottle in a ratio of 1 : 1, as shown in Fig. 3e and f. The PL peak of OAm-QDs experiences a blue-shift and the PL intensity decreases rapidly after 100 h of water treatment (Fig. S16†). Fig. S17† shows that CsOA-QDs degraded after water treatment and the PL peak blue-shifted from 513 nm to 491 nm after a month (Fig. 3e). The blue shift stems from the transfer of the 3D structure to a quasi-2D structure.[38] Finally, a white precipitate forms in the case of CsOA-QDs. For DP-QDs, after a month of water treatment, the PL peak position remains basically unchanged, the PL intensity decreases by 32% (Fig. S18†), and more than 90% of the PLQY could be retained. The water resistance mainly benefits from the protective layer. Table 1 compares the PLQY, storage stability and water resistance of PQDs prepared by our armor-like passivation strategy and other methods.

Armor-like passivation also improves the optical properties and stability of $CsPbX_3$ QDs (X = Cl or Br) prepared by this solvothermal method. Fig. S19a and c† show that the emission wavelength of $CsPbX_3$ QDs can be tuned from 411 nm to 513 nm, and the corresponding fluorescence emission changes from purple to green under 365 nm UV light. The as-synthesized DP–$CsPbX_3$ QDs exhibited the same cubic phase, size distribution (Fig. S19b and S20†) and double exponential decay (Fig. S19d†). The detailed PLQY and fluorescence decay lifetime are listed in Table S1.†

This journal is © The Royal Society of Chemistry 2021

J. Mater. Chem. A, 2021, **9**, 8772–8781 | **8777**

Table 1 Comparison of PLQY and stability of CsPbBr₃ QDs prepared by different passivation strategies

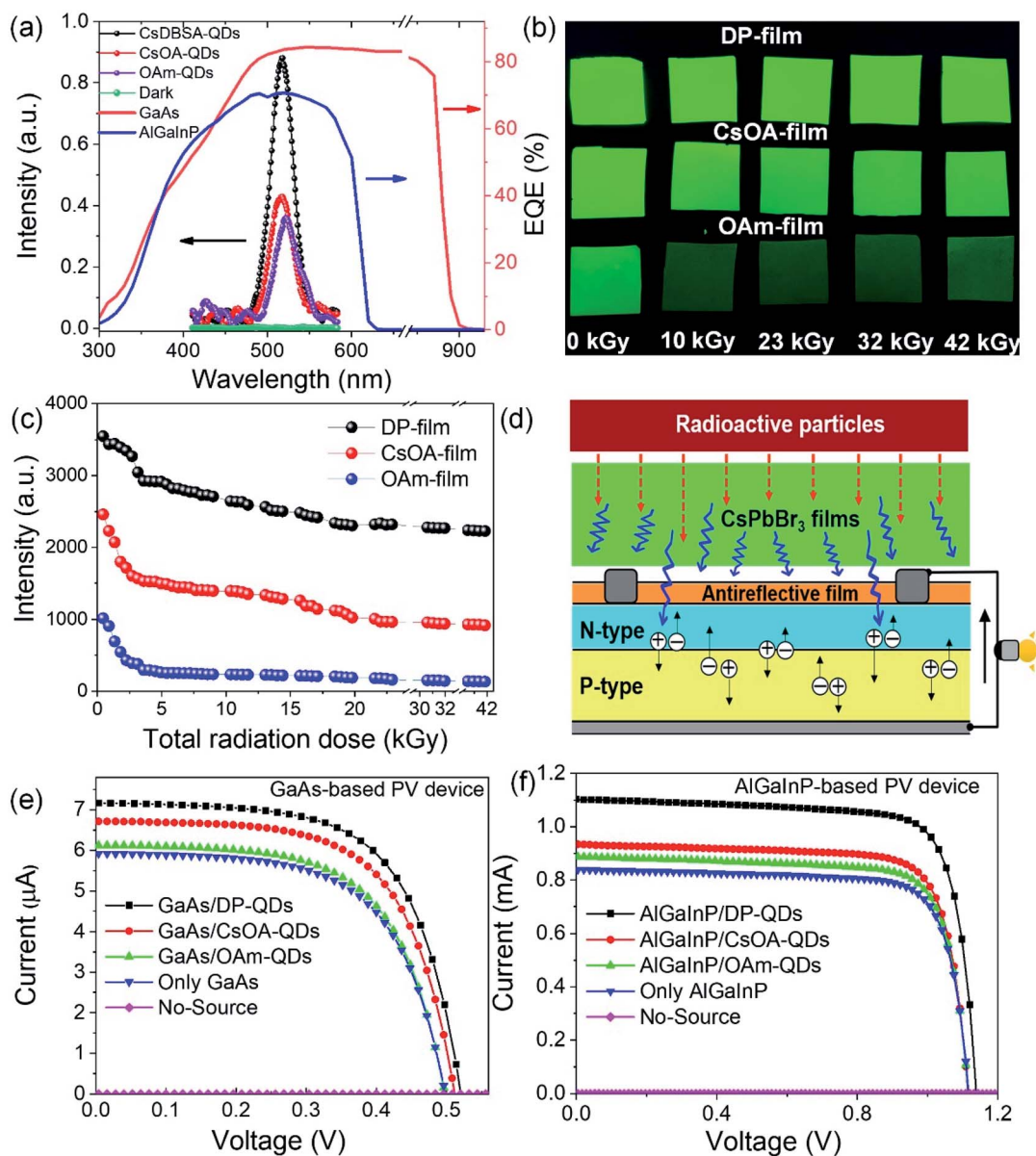| Synthesis method	Cs-precursor	PLQY (%)	Water resistance	Storage stability	Ref.
Hot-injection	Cesium 2-ethylhexanoate	80	—-	50 d	39
	CsOA	90	—	—	40
	CsDOPA	80	—	—	41
	—	90	—	5 min	25
	—	99	36 h	3 min	42
	CsOA	—	—	70 d	43
Room-temperature	—	100	60 min	—	44
Ligand exchange	CsOA	97 ± 5	—	3 weeks	16
Solvothermal	CsDBSA	97 ± 3	700 h	3 months	This work

Fig. 4 Good RL stability of PQD films and high-performance NBs. (a) RL spectra of DP-, CsOA-, and OAm-film and external quantum efficiency curves of GaAs and AlGaInP-based PV devices. (b) Luminance photos and (c) the change of the emission intensity of these films after different doses of radiation. (d) Schematic diagram of the module structure and energy conversion process of a CsPbBr₃ film based RLNB. (e) I–V characteristic curves of a GaAs-based battery and (f) AlGaInP-based battery.

8778 | *J. Mater. Chem. A*, 2021, **9**, 8772–8781

This journal is © The Royal Society of Chemistry 2021

The DP-QDs, CsOA-QDs and OAm-QDs were further prepared into films with the polymer, and their RL properties were tested. Fig. 4a shows the normalized RL emission spectra of three kinds of QD films with a thickness of 140 μm. The emission spectra of the QDs overlap with the high response band of the photovoltaic (PV) device, indicating an outstanding coupling between them and potential application of QDs in energy conversion modules. As the energy band gap of the AlGaInP-based PV device (∼2.10 eV) is higher than that of the GaAs-based PV device (∼1.42 eV), the available photon energy is also relatively higher. Taking into account the continuous radiation effect in the subsequent practical application process, long-term radiation experimental research was carried out on the three types of films. Four sets of samples were selected for each type of film to eliminate accidental errors as much as possible. Fig. 4b and c are the luminance photos of samples at different irradiation nodes, and their luminous intensity changes with the cumulative dose of irradiation. After continuous irradiation with a total dose of nearly 42 kGy (average energy of 1.25 MeV and dose rate of 0.45 kGy h^{-1}), the light intensity of DP-, CsOA- and OAm-film decreased by 36.11%, 61.83% and 86.01%, respectively. In comparison, the DP-film has the best radiation resistance. Even after such high-energy and large-dose irradiation, it can still maintain more than 60% of the initial RL strength, which means that it is feasible to use in a long-term service environment.

The whole energy conversion process of RLNBs can be divided into two stages, "radiant energy → light energy" and "light energy → electric energy". The perovskite film is used as an absorber of radioactive particles and an emitter of fluorescent photons. The working principle and overall structure of the battery are shown in Fig. 4d. GaAs-based and AlGaInP-based PV devices with anti-reflection layers were used for photoelectric conversion modules, respectively. Fig. S21† compares the maximum output power (P_{max}) of different combinations of batteries, which were obtained under the X-ray excitation with a tube voltage of 50 kV and tube current of 1 mA. The battery performance based on DP-film and CsOA-film after optimization is significantly better than that based on the OAm-film prepared by conventional methods. Compared with the traditional OAm-film, the P_{max} of the battery based on GaAs and AlGaInP PV devices has increased by 20.65% and 26.96%, respectively. The improvement of device performance is consistent with the above-mentioned optical results. For the same combination, the higher the luminous intensity of the film, the greater the output power of the battery. Fig. 4e and f show the current–voltage (I–V) characteristic curves for different combinations. When there is no excitation source, the batteries do not output electrical energy. The PV device can directly absorb radiation and convert energy through the radio-voltaic effect. Although the added perovskite film blocks and absorbs the energy of the radioactive sources to a certain extent, it compensates for this loss through the generated fluorescence, and even brings effective gains to enhance the output performance of the battery. Compared with the reference without perovskite film, the output power of RLNBs based on GaAs and AlGaInP PV devices has increased by 25.26% and 34.48%,

respectively. For the same perovskite film, the short-circuit current of the battery based on the GaAs PV device is larger, up to 6.91 μA. Correspondingly, the open-circuit voltage based on the AlGaInP PV device is larger, up to 1.14 V. This difference is mainly caused by the characteristics of the PV materials themselves. Accordingly, the energy conversion module of the battery can be adjusted independently to achieve the demand of specific electrical performance of power-consuming modules in the future. The comprehensive results show that the strategically optimized DP-film with better radiation resistance and electrical performance can be considered as an effective and suitable energy conversion material candidate in the next-generation NBs.

Conclusion

In conclusion, we propose an armor-like passivation strategy to prepare highly effective and stable PQDs *via* a solvothermal method. The rigid protection layer of the PQDs resulting from continuous ligands with strong affinity not only eliminates the surface dangling bonds and suppresses the generation of non-radiative recombination effectively, but also improves the stability of QDs significantly. The inter-ligand interaction and the binding of ligands to QDs are confirmed by IR, XPS and ^{1}H NMR data. As a result, storage stability for more than three months, high PLQY and water resistance of perovskite QDs are achieved. Furthermore, high-performance perovskite PD-films are prepared with high irradiation stability, which are used as energy conversion materials for RLNBs. Compared with the traditional OAm-film, the radiation stability of the DP-film is more than doubled, and the output power of the battery can be increased by up to 34.48%. This strategy shows intensive prospects in the field of light-emitting devices, and also provides a new method for long-life and high-reliability energy conversion systems under irradiation.

Author contributions

H. Zeng and X. Li supervised the study. D. Yang and Z. Xu were equal major contributors to this work. D. Yang conceived the idea and carried out the synthesis and characterizations of QDs. Z. Xu. fabricated and characterized the radioluminescent nuclear battery devices. C. Gong carried out the test of irradiation stability. L. Su carried out the TEM test. The manuscript was mainly written by D. Yang and Z. Xu, and revised by X. Li. All authors discussed the results and commented on the manuscript.

Conflicts of interest

There are no conflicts to declare.

Acknowledgements

This journal is © The Royal Society of Chemistry 2021

J. Mater. Chem. A, 2021, **9**, 8772–8781 | **8779**

References

1 W. Chen, X. Tang, Y. Liu, Z. Xu, Z. Han, Z. Zhang, H. Wang and C. Peng, *Int. J. Energy Res.*, 2018, **42**, 2507–2517.

2 Z. Zhang, X. Tang, Y. Liu, D. Zhou, Z. Xu, M. Wu and Z. Cao, *Energy Technol.*, 2018, **6**, 1959–1965.

3 R. Walton, C. Anthony, M. Ward, N. Metje and D. N. Chapman, *Sens. Actuators, A*, 2013, **203**, 405–412.

4 Z. H. Xu, X. B. Tang, Y. P. Liu, Z. R. Zhang, W. Chen, K. Liu and Z. C. Yuan, *ACS Appl. Mater. Interfaces*, 2019, **11**, 14191.

5 L. Protesescu, S. Yakunin, M. I. Bodnarchuk, F. Krieg, R. Caputo, C. H. Hendon, R. X. Yang, A. Walsh and M. V. Kovalenko, *Nano Lett.*, 2015, **15**, 3692.

6 X. Li, Y. Wu, S. Zhang, B. Cai, Y. Gu, J. Song and H. Zeng, *Adv. Funct. Mater.*, 2016, **26**, 2435.

7 D. Yang, X. Li, Y. Wu, C. Wei, Z. Qin, C. Zhang, Z. Sun, Y. Li, Y. Wang and H. Zeng, *Adv. Opt. Mater.*, 2019, **7**, 1900276.

8 Y. Jin, Z.-K. Wang, S. Yuan, Q. Wang, C. Qin, K.-L. Wang, C. Dong, M. Li, Y. Liu and L.-S. Liao, *Adv. Funct. Mater.*, 2020, **30**, 1908339.

9 D. Jia, J. Chen, M. Yu, J. Liu, E. M. J. Johansson, A. Hagfeldt and X. Zhang, *Small*, 2020, **16**, 2001772.

10 H. Zhao, Z. Hu, L. Wei, P. Zeng, C. Kuang, X. Liu, S. Bai, F. Gao and M. Liu, *Small*, 2020, **16**, e2003939.

11 M. Jiang, Z. Hu, L. K. Ono and Y. Qi, *Nano Res.*, 2021, **14**, 191–197.

12 Z. Wu, M. Jiang, Z. Liu, A. Jamshaid, L. K. Ono and Y. Qi, *Adv. Energy Mater.*, 2020, **10**, 1903696.

13 D. P. Nenon, K. Pressler, J. Kang, B. A. Koscher, J. H. Olshansky, W. T. Osowiecki, M. A. Koc, L. W. Wang and A. P. Alivisatos, *J. Am. Chem. Soc.*, 2018, **140**, 17760.

14 J. Pan, Y. Shang, J. Yin, M. De Bastiani, W. Peng, I. Dursun, L. Sinatra, A. M. El-Zohry, M. N. Hedhili, A. H. Emwas, O. F. Mohammed, Z. Ning and O. M. Bakr, *J. Am. Chem. Soc.*, 2018, **140**, 562.

15 J. Pradhan, P. Moitra, Umesh, B. Das, P. Mondal, G. S. Kumar, U. K. Ghorai, S. Acharya and S. Bhattacharya, *Chem. Mater.*, 2020, **32**, 7159–7171.

16 M. Imran, P. Ijaz, L. Goldoni, D. Maggioni, U. Petralanda, M. Prato, G. Almeida, I. Infante and L. Manna, *ACS Energy Lett.*, 2019, **4**, 819.

17 H. Wu, Y. Zhang, M. Lu, X. Zhang, C. Sun, T. Zhang, V. L. Colvin and W. W. Yu, *Nanoscale*, 2018, **10**, 4173.

18 J. Pan, L. N. Quan, Y. Zhao, W. Peng, B. Murali, S. P. Sarmah, M. Yuan, L. Sinatra, N. M. Alyami, J. Liu, E. Yassitepe, Z. Yang, O. Voznyy, R. Comin, M. N. Hedhili, O. F. Mohammed, Z. H. Lu, D. H. Kim, E. H. Sargent and O. M. Bakr, *Adv. Mater.*, 2016, **28**, 8718–8725.

19 Y. Shynkarenko, M. I. Bodnarchuk, C. Bernasconi, Y. Berezovska, V. Verteletskyi, S. T. Ochsenbein and M. V. Kovalenko, *ACS Energy Lett.*, 2019, **4**, 2703–2711.

20 E. Yassitepe, Z. Yang, O. Voznyy, Y. Kim, G. Walters, J. A. Castañeda, P. Kanjanaboos, M. Yuan, X. Gong, F. Fan, J. Pan, S. Hoogland, R. Comin, O. M. Bakr, L. A. Padilha, A. F. Nogueira and E. H. Sargent, *Adv. Funct. Mater.*, 2016, **26**, 8757.

21 J. De Roo, M. Ibanez, P. Geiregat, G. Nedelcu, W. Walravens, J. Maes, J. C. Martins, I. Van Driessche, M. V. Koyalenko and Z. Hens, *ACS Nano*, 2016, **10**, 2071–2081.

22 B. Zhang, L. Goldoni, J. Zito, Z. Dang, G. Almeida, F. Zaccaria, J. de Wit, I. Infante, L. De Trizio and L. Manna, *Chem. Mater.*, 2019, **31**, 9140–9147.

23 C. Wang, A. S. R. Chesman and J. J. Jasieniak, *Chem. Commun.*, 2017, **53**, 232–235.

24 S. R. Smock, T. J. Williams and R. L. Brutchey, *Angew. Chem., Int. Ed.*, 2018, **57**, 11711–11715.

25 D. Yang, X. Li, W. Zhou, S. Zhang, C. Meng, Y. Wu, Y. Wang and H. Zeng, *Adv. Mater.*, 2019, **31**, 1900767.

26 Z. Shi, S. Li, Y. Li, H. Ji, X. Li, D. Wu, T. Xu, Y. Chen, Y. Tian, Y. Zhang, C. Shan and G. Du, *ACS Nano*, 2018, **12**(2), 1462–1472.

27 F. Krieg, Q. K. Ong, M. Burian, G. Raino, D. Naumenko, H. Amenitsch, A. Süess, M. Grotevent, F. Krumeich, M. I. Bodnarchuk, I. Shorubalko, F. Stellacci and M. V. Kovalenko, *J. Am. Chem. Soc.*, 2019, **141**(50), 19839–19849.

28 G. Almeida, L. Goldoni, Q. Akkerman, Z. Dang, A. H. Khan, S. Marras, I. Moreels and L. Manna, *ACS Nano*, 2018, **12**, 1704–1711.

29 T. Ahmed, S. Seth and A. Samanta, *Chem. Mater.*, 2018, **30**, 3633–3637.

30 F. Li, Y. Liu, H. Wang, Q. Zhan, Q. Liu and Z. Xia, *Chem. Mater.*, 2018, **30**, 8546–8554.

31 Z. Li, L. Kong, S. Huang and L. Li, *Angew. Chem., Int. Ed.*, 2017, **56**, 8134–8138.

32 J. Zhuang, M. Li, Y. Pu, A. J. Ragauskas and C. G. Yoo, *Appl. Sci.*, 2020, **10**(12), 4345.

33 J. S. Singh, *Spectrosc. Lett.*, 2008, **41**, 122–127.

34 J. Joo, T. Yu, Y. W. Kim, H. M. Park, F. Wu, J. Z. Zhang and T. Hyeon, *J. Am. Chem. Soc.*, 2003, **125**, 6553–6557.

35 G. Huang, C. Wang, H. Zhang, S. Xu, Q. Xu and Y. Cui, *J. Mater. Chem. A*, 2018, **6**, 2449–2455.

36 J. Pan, Y. Shang, J. Yin, M. De Bastiani, W. Peng, I. Dursun, L. Sinatra, A. M. El-Zohry, M. N. Hedhili, A.-H. Emwas, O. F. Mohammed, Z. Ning and O. M. Bakr, *J. Am. Chem. Soc.*, 2018, **140**, 562–565.

37 Y. Cao, A. Stavrinadis, T. Lasanta, D. So and G. Konstantatos, *Nat. Energy*, 2016, **1**, 16035.

38 M. C. Brennan, J. E. Herr, T. S. Nguyen-Beck, J. Zinna, S. Draguta, S. Rouvimov, J. Parkhill and M. Kuno, *J. Am. Chem. Soc.*, 2017, **139**, 12201–12208.

39 F. Krieg, S. T. Ochsenbein, S. Yakunin, S. ten Brinck, P. Aellen, A. Suess, B. Clerc, D. Guggisberg, O. Nazarenko, Y. Shynkarenko, S. Kumar, C.-J. Shih, I. Infante and M. V. Kovalenko, *ACS Energy Lett.*, 2018, **3**, 641–646.

40 Y. Tan, Y. Zou, L. Wu, Q. Huang, D. Yang, M. Chen, M. Ban, C. Wu, T. Wu, S. Bai, T. Song, Q. Zhang and B. Sun, *ACS Appl. Mater. Interfaces*, 2018, **10**, 3784.

41 Y. Shynkarenko, M. I. Bodnarchuk, C. Bernasconi, Y. Berezovska, V. Verteletskyi, S. T. Ochsenbein and M. V. Kovalenko, *ACS Energy Lett.*, 2019, **4**, 2703.

42 S. Paul and A. Samanta, *ACS Energy Lett.*, 2020, **5**, 64–69.

43 D. Yan, T. Shi, Z. Zang, T. Zhou, Z. Liu, Z. Zhang, J. Du, Y. Leng and X. Tang, *Small*, 2019, **15**, 1901173.

44 Q. Zhong, M. Cao, Y. Xu, P. Li, Y. Zhang, H. Hu, D. Yang, Y. Xu, L. Wang, Y. Li, X. Zhang and Q. Zhang, *Nano Lett.*, 2019, **19**, 4151.

This journal is © The Royal Society of Chemistry 2021

J. Mater. Chem. A, 2021, **9**, 8772–8781 | **8781**